




Enhancing Damping in Single-Phase Grid-Forming Virtual Oscillator Control Inverters: A Feedforward Strategy

HAMED REZAZADEH ¹, MOHAMMAD MONFARED ¹ (Senior Member, IEEE),
MEGHAD FAZELI ¹ (Senior Member, IEEE), AND SAEED GOLESTAN² (Senior Member, IEEE)

¹Department of Electronic and Electrical Engineering, Swansea University, SA1 8EN Swansea, U.K.

²AAU Energy, Aalborg University, 9220 Aalborg East, Denmark

CORRESPONDING AUTHOR: MOHAMMAD MONFARED (e-mail: mohammad.monfared@swansea.ac.uk).

ABSTRACT The expansion of residential distributed generation systems relies heavily on single-phase inverters for grid integration. However, these inverter-based resources compromise grid stability, mainly due to a lack of inertia and grid strength. To address these issues, grid-forming inverters have been developed, with virtual oscillator control (VOC) emerging as a promising approach due to its superior dynamic performance. However, basic VOC-based inverters cannot provide inertial functionality. Attempts to incorporate virtual inertia into VOCs have significantly reduced the damping factor and led to severe dynamic oscillations. This article presents a novel technique to improve the dynamic response of single-phase VOC-based inverters by enhancing damping without affecting the virtual inertia and droop functionalities. The effectiveness of the proposed approach is validated through small-signal analysis and extensive experimental testing on a 2.5 kVA single-phase inverter. The results confirm the small-signal model with well-damped dynamic responses in grid-connected mode, without degrading system inertia during stand-alone operation.

INDEX TERMS Damping control, grid-forming (GFM) inverter, single-phase inverter, virtual inertia, virtual oscillator control (VOC).

NOMENCLATURE

AHO	Andronov–Hopf oscillator.	VSG	Virtual synchronous generator.
FLL	Frequency-locked loop.	VOC	Virtual oscillator control.
GFL	Grid-following.	μ	AHO voltage magnitude gain.
GFM	Grid-forming.	η	AHO current tracking gain.
IBRs	Inverter-based resources.	φ	AHO droop inductive/resistive control parameter.
LPF	Low-pass filter.	P_0/Q_0	Nominal active/reactive power.
OS	Overshoot.	$P_{\text{ref}}/Q_{\text{ref}}$	Active/reactive power reference.
PR	Proportional-resonant controller.	T_f, ω_f	Virtual inertia (R controller) control gain ($\omega_f = 1/T_f$).
PRR	Proportional-resonant-resonant controller.	K_p	PR controller proportional gain.
PWM	Pulsewidth modulation.	T_i, ω_i	Virtual inertia (PRR controller) control gain ($\omega_i = 1/T_i$).
R	Resonant controller.	K_{so}	SOGI gain.
RoCoF	Rate of change of frequency.	T_{so}	SOGI equivalent inertial time constant.
SG	Synchronous generator.	ξ	Damping factor.
SOGI	Second-order generalized integrator.	ω_{n1}	Proposed controller natural frequency set-point in response to power reference step changes.
THD	Total harmonic distortion.		
US	Undershoot.		
uVOC	Unified VOC.		

ω_{n2}	Proposed controller natural frequency setpoint in response to grid frequency step changes.
K_{p-FLL}	SOGI-FLL proportional gain.
K_{i-FLL}	SOGI-FLL integral gain.
ξ_{FLL}	SOGI-FLL damping factor setpoint.
ω_{n-FLL}	SOGI-FLL natural frequency setpoint.

I. INTRODUCTION

With the increasing integration of inverter-based resources (IBRs) in power generation, power systems are encountering new stability challenges due to the reduced system inertia. This reduction can result in a higher rate of change of frequency (RoCoF) and a lower frequency nadir, both of which jeopardize grid stability. To address these challenges, grid-forming (GFM) control has emerged as a pivotal solution to enhance grid stability and resilience. Unlike grid-following (GFL) control, which operates IBRs as current sources, GFM inverters function as voltage sources, enabling their use in stand-alone applications and making them well-suited for weak grid conditions [1], [2].

Two common GFM implementation strategies are synchronous generator (SG) emulation-based methods and oscillator-based methods [3]. The former includes droop control, virtual SG (VSG), synchronverter, power synchronization control, and synchronous power control [4]. The latter, mainly known as virtual oscillator control (VOC), is an emerging strategy that has shown superior dynamic performance compared to SG emulation-based methods. Thanks to their time-domain implementation, VOCs offer several advantages, including fast synchronization, no need for explicit power calculations, and a reduced computational burden compared to SG emulation-based techniques, making them a practical choice for implementation at the distributed generation or power system level [5], [6]. VOC emulates the dynamic behavior of nonlinear oscillators, such as dead-zone [7], Van der Pol [8], and Andronov–Hopf [9], [10]. Among these, the Andronov–Hopf oscillator (AHO) stands out for its dispatchability and ability to generate a harmonic-free voltage waveform, making it well-suited for grid-connected applications [11]. The unified VOC (uVOC), as a successful AHO-based strategy, has been proposed for GFM and GFL applications, which can be applied to both three-phase and single-phase converters [12].

Despite the advantages of VOC-based inverters, their lack of inherent virtual inertia poses a significant limitation. Early attempts to address this include a proportional-derivative controller designed to adjust the power setpoint based on frequency variations [13], [14], [15]. However, the derivative action reduces noise immunity, making it less practical. The method proposed in [16] introduced inertial response by applying a low-pass filter (LPF) to the calculated active and reactive power of the uVOC, which is similar to the approach used to provide virtual inertia in conventional droop control [17]. However, this approach requires power calculations, which may increase the computational complexity and reduce synchronization speed. This challenge is

especially pronounced in single-phase systems, where instantaneous power is oscillatory and difficult to calculate. The use of a resonant (R) controller in the current control loop of AHO-based inverters has been proposed as an alternative, offering inertia emulation [18]. It has been demonstrated that using a resonant controller for current is analogous to applying an LPF to power in AHO-based inverters. While all these methods offer some sort of inertial response, they result in a reduced damping factor, leading to significant oscillations and over/undershoot (OS/US) in power and current waveforms. Such oscillations are particularly problematic for GFM inverters, which have limited overcurrent capabilities, increasing the risk of damage or unnecessary tripping [19]. To address these, proportional-resonant (PR) and proportional-resonant-resonant (PRR) controllers have been proposed [18]. These methods modify the dynamic response of VOC-based inverters by adding a zero to their transfer functions, at the cost of reduced inertia in stand-alone mode. Furthermore, the damping factor of these methods remains tied to the droop control parameter of VOC, requiring a tradeoff between improved damping and adequate virtual inertia and droop coefficients.

Damping enhancement methods for well-established VSGs, including feedback and feedforward approaches, have been widely explored in [20]. Feedforward methods, in particular, enhance damping without sacrificing virtual inertia [21]. However, adapting such approaches to VOCs has been underexplored, primarily due to the inherent differences in their control implementation compared to VSGs.

Despite advancements in single-phase GFM inverters, research has been predominantly focused on three-phase systems. Single-phase GFM implementation presents unique challenges, including double-frequency power oscillations and the need for orthogonal signal generation [22], [23], [24]. Specifically, since AHO control is implemented in the alpha-beta ($\alpha\beta$) reference frame, a quadrature signal should be generated for the measured current in single-phase inverters. In [12], a time delay of $1/(4f_0)$ (where f_0 is the grid's nominal frequency) is used to create this orthogonal signal in single-phase uVOC. However, grid frequency deviations in GFM applications may lead to nonorthogonality between $\alpha\beta$ components. As a viable alternative, a second-order generalized integrator (SOGI)-based quadrature signal generator, referred to simply as SOGI in this article, has been successfully utilized in [23]. Although adopting SOGI improves accuracy, it also affects the dynamic response of the inverter, which has been simply neglected in the literature.

To address these gaps, this article proposes a new feedforward damping improvement strategy for single-phase VOC-based inverters, which effectively mitigates oscillations caused by both active power setpoint changes and grid frequency variations without degrading virtual inertia. To implement the grid frequency feedforward, a SOGI frequency-locked loop (SOGI-FLL) is employed to measure the grid frequency. Through mathematical analysis, the inertial effect of orthogonal signal generation using an SOGI is derived and validated through experimental tests. An accurate small-signal

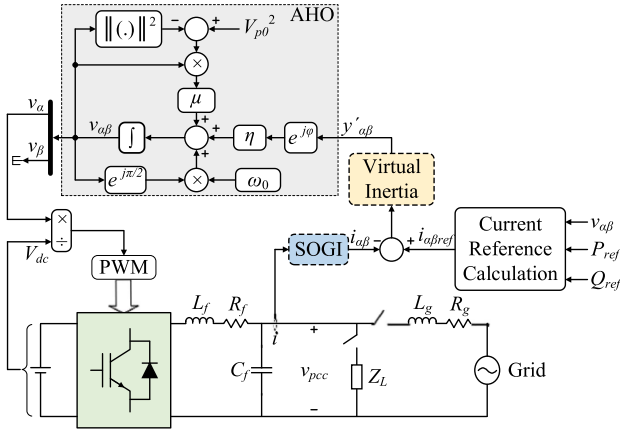


FIGURE 1. Single-phase AHO-based inverter with virtual inertia.

model, incorporating both the SOGI inertial effect and the influence of SOGI-FLL, is developed, which allows the design of a superior damping strategy. The proposed approach allows for independent and flexible tuning of damping, inertia, and droop coefficients to meet system requirements straightforwardly. Small-signal stability analysis confirms that the proposed strategy does not compromise the stability of the conventional controller. Extensive testing on a 2.5 kVA single-phase inverter, in both grid-connected and stand-alone modes, validates the effectiveness of the proposed strategy in minimizing power overshoot and oscillations while improving frequency transient behavior.

The rest of the article is organized as follows. Section II provides a review of the single-phase AHO-based inverter with virtual inertia. Section III investigates the effect of SOGI on inverter dynamics and proposes a new damping improvement strategy, with experimental validation of the theoretical results presented in Section IV. Finally, Section V concludes the article.

II. DAMPING ANALYSIS OF THE SINGLE-PHASE AHO-BASED INVERTER

Fig. 1 shows the single-phase implementation of the uVOC-based inverter presented in [12], incorporating the virtual inertia strategy from [18]. Since uVOC is an implementation of the AHO strategy, this article refers to the control scheme as the AHO-based strategy. The power circuit consists of a dc power source, a single-phase inverter, and an LC filter (L_f and C_f) connected to the local load (Z_L) and grid with the inductance (L_g) and the resistance (R_g). In this figure, v_{pcc} represents the voltage at the point of common coupling. Unlike GFL applications, the DC-link voltage of the GFM inverter is regulated by a front-end converter or an energy storage unit. Thus, a constant DC-link voltage is assumed in this article [25].

The AHO is a nonlinear time-domain controller implemented in the $\alpha\beta$ reference frame. The control law of the oscillator output voltage, without considering the virtual

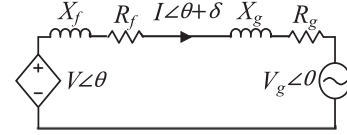


FIGURE 2. Simplified model of a single-phase inverter connected to the grid.

inertia and SOGI, is given by the following equation [12]:

$$\begin{bmatrix} \dot{v}_\alpha \\ \dot{v}_\beta \end{bmatrix} = \begin{bmatrix} \mu (V_{p0}^2 - V_p^2) & -\omega_0 \\ \omega_0 & \mu (V_{p0}^2 - V_p^2) \end{bmatrix} \begin{bmatrix} v_\alpha \\ v_\beta \end{bmatrix} + \eta \begin{bmatrix} \cos \varphi & -\sin \varphi \\ \sin \varphi & \cos \varphi \end{bmatrix} \begin{bmatrix} i_{\alpha ref} - i_\alpha \\ i_{\beta ref} - i_\beta \end{bmatrix}. \quad (1)$$

In (1), v_α and v_β represent the oscillator output voltages. Taking an average over a switching period, the switching network with the DC-link voltage normalization can be approximated as a unity-gain block [12]. Thus, v_α can be assumed as the inverter's output voltage. Moreover, $i_{\alpha ref}$ and $i_{\beta ref}$ are the inverter's reference currents, i_α and i_β are the inverter's output currents in the $\alpha\beta$ reference frame, ω_0 is the grid nominal angular frequency, and V_{p0} is the nominal value of the voltage vector magnitude V_p . Additionally, μ is the voltage magnitude gain, which controls the convergence speed of the oscillator; η represents the current tracking gain, and φ sets the inductive/resistive droop characteristic [12]. These parameters can be adjusted based on the design procedure developed in [12]. Specifically, η and μ are selected to support the nominal active power (P_0) and reactive power (Q_0) for the maximum allowable deviation in grid frequency ($\Delta f_{g,max}$) and a 5% change in voltage amplitude. The National Grid Electricity System Operator for Great Britain specifies $\Delta f_{g,max} = 0.5$ Hz [26]. The parameter φ can be adjusted to provide the desired droop functionality, which can be either $\varphi = 0$ for resistive (f - Q and v - P droop) or $\varphi = \pi/2$ for inductive (f - P and v - Q droop). Fig. 2 shows the simplified model of the GFM power converter connected to a grid. In this model, V and V_g represent the root mean square (RMS) values of the inverter output and grid voltages, respectively. The phase-angle difference between them is denoted as θ , whereas δ represents the phase-angle difference between the inverter's output voltage and current. Due to its small value, the effect of the filter capacitance is ignored. According to this model, the output active (P) and reactive (Q) powers of the inverter can be calculated as

$$P = \frac{V}{R_T^2 + X_T^2} [R_T (V - V_g \cos \theta) + X_T V_g \sin \theta] \quad (2a)$$

$$Q = \frac{V}{R_T^2 + X_T^2} [X_T (V - V_g \cos \theta) - R_T V_g \sin \theta] \quad (2b)$$

where $R_T = R_f + R_g$, $X_T = \omega_0 (L_f + L_g)$. According to the parameters in Table 1, $R_g/X_g = 3.2$, which is within the acceptable range for low- and medium-voltage utility grids [27]. This gives $R_T/X_T = 0.39$. Thus, (2) can be approximated

TABLE 1. Experimental Parameters

Parameters	Description	Value
P_0	Rated active power	2000 W
Q_0	Rated reactive power	1500 var
V_{dc}	DC-link voltage	380 V
ω_0	Nominal angular frequency	$2\pi \times 50$ rad/s
V_{p0}	Nominal voltage amplitude	311 V
f_s	Switching frequency	20 kHz
L_f, R_f	Filter impedance	7 mH, 0.08 Ω
C_f	Filter capacitance	3.9 μ F
L_g, R_g	Grid impedance	1 mH, 1 Ω
R_{L1}, R_{L2}	Local loads	100 Ω , 33 Ω
μ	AHO voltage magnitude gain	2.38×10^{-4}
η	AHO current tracking gain	83.82
T_f	Virtual inertia control parameter	$1/(2\pi)$
K_p	PR controller proportional gain	0.6
K_{ω}	SOGI gain	0.707
ζ_{FLL}	SOGI-FLL damping factor setpoint	0.9
ω_{n-FLL}	SOGI-FLL natural frequency setpoint	150 rad/s
ζ	Proposed controller damping factor setpoint	0.85
ω_{n1}, ω_{n2}	Proposed controller natural frequency setpoints	$2\pi, 4\pi$ rad/s

by (3), showing that P and Q are primarily regulated by phase-angle difference and voltage amplitude, respectively. As a result, $\varphi = \pi/2$ is chosen for the rest of the study.

$$P \approx \frac{VV_g}{X_T} \theta = K_s \theta \quad (3a)$$

$$Q \approx \frac{V}{X_T} (V - V_g). \quad (3b)$$

By defining $\theta = \arctan(v_\beta/v_\alpha)$ and neglecting the SOGI inertial effect, the voltage amplitude and phase angle dynamics of the oscillator's output voltage can be expressed as [12]

$$\dot{\theta} = \omega = \omega_0 + \frac{2\eta}{V_p^2} (P_{ref} - P) = \omega_0 + D (P_{ref} - P) \quad (4a)$$

$$\dot{V}_p = \mu V_p (V_{p0}^2 - V_p^2) + \frac{2\eta}{V_p} (Q_{ref} - Q) \quad (4b)$$

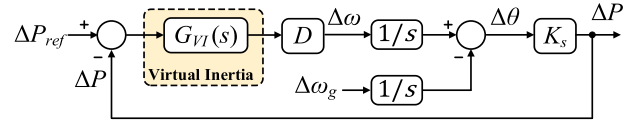
where ω is the inverter's angular frequency and P_{ref} and Q_{ref} are the active and reactive power reference values, respectively.

To introduce virtual inertia into the VOC's dynamic response, various combinations of proportional-resonant controllers have been implemented, including R, PR, and PRR controllers for the current error in the $\alpha\beta$ frame, with the corresponding transfer functions given in the following equations [18]:

$$G_R(s) = \frac{2\omega_f s}{s^2 + 2\omega_f s + \omega_0^2} \quad (5a)$$

$$G_{PR}(s) = K_p + (1 - K_p) \frac{2\omega_f s}{s^2 + 2\omega_f s + \omega_0^2} \quad (5b)$$

$$G_{PRR}(s) = G_{PR}(s) \frac{2\omega_i s}{s^2 + 2\omega_i s + \omega_0^2} \quad (5c)$$


FIGURE 3. Small-signal model of conventional AHO-based inverter [18].

where $G_R(s)$, $G_{PR}(s)$, and $G_{PRR}(s)$ are the transfer functions of the R, PR, and PRR controllers, respectively, $\omega_f = 1/T_f$ and $\omega_i = 1/T_i$ are the resonant control parameters to provide virtual inertia, and K_p is the PR proportional gain, which mainly contributes to damping. It has been shown that the dynamics of the phase angle can be represented as the general form given in the following equation [18]:

$$\dot{\theta} = \omega = \omega_0 + G_{VI}(s) D (P_{ref} - P) \quad (6)$$

where \bar{x} denotes the average value of the parameter x and $G_{VI}(s)$ is given in the following equation for different controllers:

$$G_{VI}(s) = \begin{cases} \frac{1}{T_f s + 1}, & \text{R} \\ \frac{K_p T_f s + 1}{T_f s + 1}, & \text{PR} \\ \frac{K_p T_f s + 1}{T_f s + 1} \frac{1}{T_i s + 1}, & \text{PRR} \end{cases} \quad (7)$$

The derivation of (6) and $G_{VI}(s)$ in (7) is provided in Appendix A.

The small-signal model of the single-phase AHO-based inverter with added virtual inertia can be obtained from (6), as shown in Fig. 3 [18]. Based on this model, the transfer functions of $\Delta P(s)/\Delta P_{ref}(s)$ and $\Delta P(s)/\Delta \omega_g(s)$ are given in the following equations:

$$\frac{\Delta P(s)}{\Delta P_{ref}(s)} = \frac{G_{VI}(s) D K_s}{s + G_{VI}(s) D K_s} \quad (8a)$$

$$\frac{\Delta P(s)}{\Delta \omega_g(s)} = -\frac{K_s}{s + G_{VI}(s) D K_s} \quad (8b)$$

where ω_g is the grid angular frequency, and $K_s = V V_g / X_T$ and $D = 2\eta / V_p^2$ can be obtained from (3a) and (4a), respectively.

Furthermore, the transfer function of $\Delta \omega(s)/\Delta P(s)$ in stand-alone mode is

$$\frac{\Delta \omega(s)}{\Delta P(s)} = -G_{VI}(s) D. \quad (9)$$

In this article, the parameters of the conventional and proposed controllers are designed to align with the practical limitations of the power electronic converters and the requirements set by the grid operator, based on the following two key practical criteria.

- 1) Power OS, which is limited by the thermal and electrical constraints of the power electronic components. In practice, converters are typically designed to withstand up to 20% overcurrent for short durations.
- 2) RoCoF, which is dictated by the grid requirements. Most grid operators limit RoCoF to values between 1 and 3.5 Hz/s [28], [29], [30].

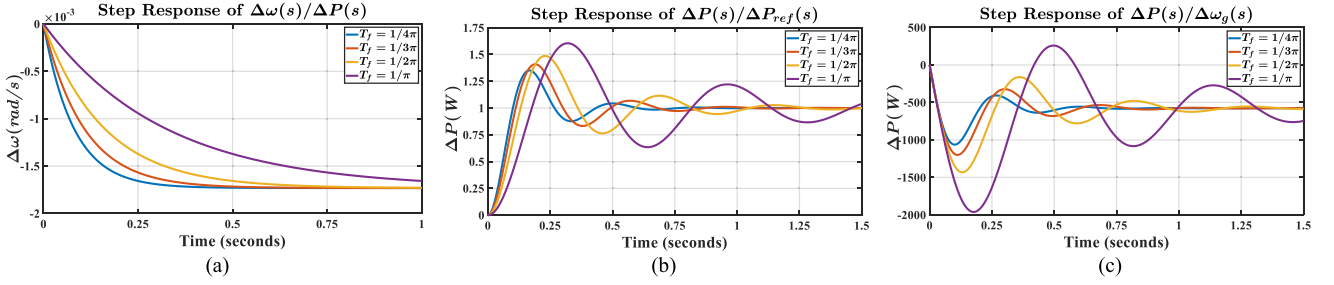


FIGURE 4. Step response of the conventional R controller for various T_f . (a) $\Delta\omega(s)/\Delta P(s)$. (b) $\Delta P(s)/\Delta P_{ref}(s)$. (c) $\Delta P(s)/\Delta\omega_g(s)$.

To provide sufficient virtual inertia, the parameter T_f of the conventional R controller should be designed to meet the desired RoCoF requirement. The RoCoF is defined as the RoCoF in response to load change and can be calculated using the following equation:

$$\text{RoCoF} = \frac{d\Delta f}{dt} = \frac{1}{2\pi} \frac{d\Delta\omega}{dt}. \quad (10)$$

For the R controller, the change of the angular frequency in response to a load step change of ΔP can be obtained from (7) and (9) as

$$\Delta\omega(s) = -\frac{\Delta P}{s} \frac{D}{T_f s + 1}. \quad (11)$$

Then, $\Delta\omega(t)$ can be obtained by taking the inverse Laplace transform. Substituting $\Delta\omega(t)$ in (10) results in the following equation:

$$\text{RoCoF} = -\frac{D\Delta P}{2\pi T_f} (e^{-t/T_f}). \quad (12)$$

Equation (12) explicitly shows that the RoCoF depends on D and T_f . Increasing D leads to a higher RoCoF by amplifying the frequency change in response to a power variation. Conversely, increasing T_f reduces RoCoF due to its virtual inertial effect.

Two well-known methods for estimating RoCoF in systems with an LPF response are the 60 ms method and the automatic control theorem method, with the corresponding equations, respectively [30]

$$\text{RoCoF} = \frac{f_{(t=0)} - f_{(t=60 \text{ ms})}}{0.06} = \frac{D\Delta P}{2\pi \times 0.06} (1 - e^{-0.06/T_f}) \quad (13a)$$

$$\text{RoCoF} = \frac{D\Delta P}{2\pi T_f}. \quad (13b)$$

The maximum RoCoF occurs when ΔP equals the nominal active power (2 kW). Considering $D = 2\eta/V_p^2$ and according to the parameters in Table 1, one obtains $D\Delta P \approx 3.4$. Thus, by selecting $T_f = 1/(2\pi)$, the maximum of RoCoF is approximately 3.4 Hz/s, which lies within the acceptable range.

Substituting $G_{VI}(s)$ from (7) into (8) results in second-order transfer functions for the R controller. From this transfer function, the damping factor (ξ) is calculated in the following

equation:

$$\xi = \frac{1}{2} \frac{1}{\sqrt{T_f D K_s}}. \quad (14)$$

Equation (14) highlights that the damping factor of the R controller depends on the virtual inertia (T_f), droop (D), and grid parameters (K_s). Increasing T_f to enhance virtual inertia reduces the damping factor, leading to oscillatory behavior.

The step responses of the transfer functions in (8) and (9) are shown in Fig. 4 for the R controller with different values of T_f [18]. These figures illustrate that while the R controller provides sufficient inertia, as observed in Fig. 4(a), it reduces the damping factor, resulting in a high OS/US and considerable power oscillations, as shown in Fig. 4(b) and (c). For the designed value $T_f = 1/(2\pi)$, considering 2 kW as the maximum allowable change in active power, the maximum RoCoF can be calculated from Fig. 4(a) as 3.3 Hz/s, within the acceptable range. However, the corresponding power OS and US values in Fig. 4(b) and (c) are 48% and 143%, respectively, which exceed the practical limit, indicating the need for improved damping strategies. At $T_f = 1/(4\pi)$, both the RoCoF and OS/US exceed acceptable limits. While $T_f = 1/(2\pi)$ and $T_f = 1/\pi$ provide acceptable RoCoF values, $T_f = 1/(2\pi)$ results in a lower power OS/US and is thus selected.

To improve the damping performance of the conventional R controller, a PR controller has been proposed in [18]. The damping factor of the PR controller can be obtained from the transfer functions in (8), as

$$\xi = \frac{1}{2} \left(\frac{1}{\sqrt{T_f D K_s}} + K_p \sqrt{T_f D K_s} \right). \quad (15)$$

Equation (15) indicates that increasing K_p enhances the damping. Here, T_f is retained to ensure sufficient virtual inertia [18]. Therefore, tuning K_p is key to reducing power OS/US. However, the calculated $\Delta\omega(s)/\Delta P(s)$ in (16) shows that an increase in K_p introduces an additional zero, which reduces the effective virtual inertia. Moreover, evaluating the initial frequency deviation yields $\Delta\omega_{(0+)} = DK_p$. This result shows that a higher K_p causes a larger initial frequency jump. Therefore, while increasing K_p improves damping, it also compromises inertial performance.

$$\frac{\Delta\omega(s)}{\Delta P(s)} = -\frac{D(K_p T_f s + 1)}{T_f s + 1}. \quad (16)$$

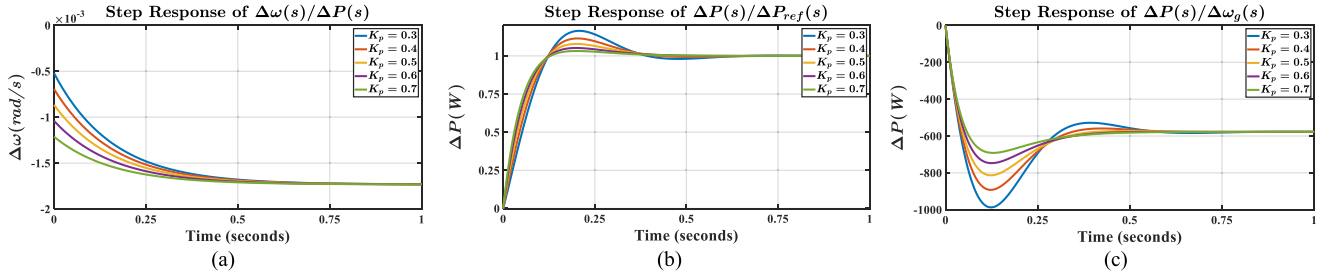


FIGURE 5. Step response of the conventional PR controller for various K_p . (a) $\Delta\omega(s)/\Delta P(s)$. (b) $\Delta P(s)/\Delta P_{\text{ref}}(s)$. (c) $\Delta P(s)/\Delta\omega_g(s)$.

The parameter K_p should be designed to achieve a satisfactory power OS/US. To do this, step responses of the PR controller for different values of K_p are plotted in Fig. 5. Fig. 5(a) shows a degraded virtual inertia with a higher RoCoF compared to the conventional R controller. However, both $\Delta P(s)/\Delta P_{\text{ref}}(s)$ and $\Delta P(s)/\Delta\omega_g(s)$ in Fig. 5(b) and (c) exhibit acceptable power OS for $K_p \geq 0.6$. Although the power US for $\Delta P(s)/\Delta\omega_g(s)$ slightly exceeds 20% at $K_p = 0.6$, this is considered acceptable because experimental power OS/US values are typically lower due to parasitic resistances. At $K_p = 0.7$, although power OS/US improves, the RoCoF becomes unacceptably high, and at $K_p = 0.5$, power OS/US remains above the 20% threshold. Therefore, $K_p = 0.6$ is selected as a balanced compromise between damping improvement and RoCoF degradation.

Finally, the PRR controller has been introduced as a compromise between the R and PR controllers. However, this controller exhibits lower damping and virtual inertia compared to the PR and R methods, respectively [18].

In summary, the damping factor of these methods remains highly dependent on the droop coefficient (D) of the VOC [18]. This means that a coupling exists between virtual inertia, damping factor, and droop capability in the conventional AHO-based inverter with added virtual inertia, leading to a tradeoff between these ancillary services during parameter design. This indicates that a more advanced damping strategy is required to meet both OS/US and RoCoF criteria.

III. PROPOSED DAMPING IMPROVEMENT STRATEGY

To address the challenges discussed in Section II, this article proposes a new damping improvement strategy that allows the damping factor to be adjusted independently of both virtual inertia and droop coefficient. To achieve this, the effect of SOGI on the small-signal model is first investigated.

A. EFFECT OF SOGI ON THE VOC'S DYNAMIC BEHAVIOR

In single-phase systems, the VOC requires transforming the measured current into the $\alpha\beta$ reference frame using a SOGI. The transfer function between the α -axis output of the SOGI and its input is given as

$$\frac{i_\alpha(s)}{i(s)} = \frac{K_{so}\omega s}{s^2 + K_{so}\omega s + \omega^2} \quad (17)$$

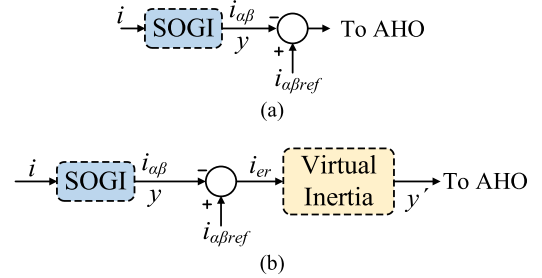


FIGURE 6. Relationship between measured current and AHO's input with (a) SOGI effect and (b) both SOGI and virtual inertia effects.

where K_{so} is the SOGI gain and is set to $K_{so} = 0.707$ to provide a balance between bandwidth and noise immunity [31]. Following a similar procedure used for resonant controllers in [18], the dynamic effect of SOGI on VOCs can be studied. A state-space equivalent of (17) can be written as

$$\begin{cases} \dot{x}_1 = \omega x_2 \\ \dot{x}_2 = -\omega x_1 - K_{so}\omega x_2 + K_{so}\omega i \\ y = x_2 \end{cases} \quad (18)$$

where $x_1 = X\sin(\gamma)$, $x_2 = X\cos(\gamma)$, and $i = I\cos(\gamma)$. Fig. 6(a) shows the relationship between the measured current (i) and AHO's input, where y is the output of the SOGI. Here, it is assumed that the input and α -axis output signals of SOGI remain sinusoidal and in phase. Then, the dynamic equation for the states' amplitude (X) can be obtained using the polar coordinate transformation as

$$\dot{X} = -K_{so}\omega X\cos^2(\gamma) + K_{so}\omega I\cos^2(\gamma). \quad (19)$$

By averaging over one AC cycle, and considering $Y=X$ from (18), the relationship between the output and input signal amplitudes simplifies to

$$\frac{\bar{Y}(s)}{\bar{I}(s)} = \frac{K_{so}\omega/2}{s + K_{so}\omega/2} = \frac{1}{T_{so}s + 1}. \quad (20)$$

The low-pass filtering effect of (20) implies an inertial effect between the input and output signal amplitudes. From Fig. 1, the control law of AHO was obtained in (1). By considering the SOGI effect and defining $v_\alpha = V_p\cos(\theta)$, $v_\beta = V_p\sin(\theta)$, $y_\alpha = Y\cos(\theta + \delta)$, and $y_\beta = Y\sin(\theta + \delta)$, (1) can be

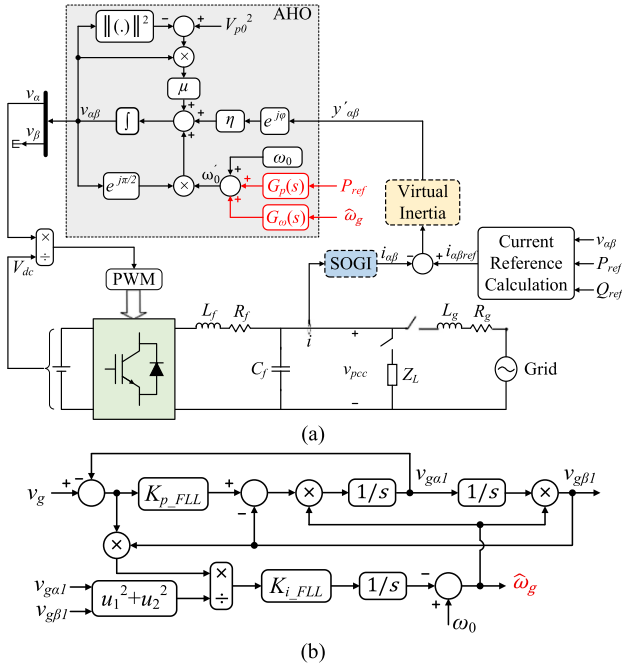


FIGURE 7. (a) Overall block diagram of the proposed damping strategy. (b) SOGI-FLL block diagram [31].

rewritten as

$$\begin{cases} \dot{v}_\alpha = \mu (V_{p0}^2 - V_p^2) v_\alpha - \omega_0 v_\beta - \eta (i_{\beta ref} - y_\beta) \\ \dot{v}_\beta = \omega_0 v_\alpha + \mu (V_{p0}^2 - V_p^2) v_\beta + \eta (i_{\alpha ref} - y_\alpha) \end{cases} \quad (21)$$

By defining $\theta = \arctan(v_\beta / v_\alpha)$, its time derivative can be expressed as

$$\dot{\theta} = \frac{\dot{v}_\beta v_\alpha - v_\beta \dot{v}_\alpha}{V_p^2}. \quad (22)$$

Substituting (21) into (22) and averaging over one AC cycle yields

$$\dot{\theta} = \omega_0 + \frac{2\eta}{V_p^2} P_{ref} - \frac{\eta \bar{Y}}{V_p} \cos(\delta) \quad (23)$$

where $P_{ref} = 0.5(v_\alpha i_{\alpha ref} + v_\beta i_{\beta ref})$. Substituting \bar{Y} from (20) in (23) results in

$$\dot{\theta} = \omega = \omega_0 + D \left(P_{ref} - \frac{1}{T_{so} s + 1} P \right) \quad (24)$$

where $P = 0.5 V_p \bar{I} \cos(\delta)$. Equation (24) shows that the SOGI's effect on the AHO's dynamic response is similar to the use of an LPF with T_{so} time constant for power in the droop equation.

B. PROPOSED STRATEGY

A feedforward damping strategy is proposed in this article for the AHO-based inverter without degrading the inertial response. As shown in Fig. 7(a), it is proposed that the oscillator's angular frequency deviates from its nominal value to oppose the oscillations caused by the changes in either power

reference or grid frequency. Thus, the oscillator's angular frequency in (1) is modified as

$$\omega'_0 = \omega_0 + G_p(s) P_{ref} + G_\omega(s) \hat{\omega}_g \quad (25)$$

where $G_p(s)$ and $G_\omega(s)$ mitigate oscillations induced by variations in P_{ref} and ω_g , respectively, and $\hat{\omega}_g$ is the estimated grid angular frequency. In the proposed strategy, the input to $G_\omega(s)$ is provided from a SOGI-FLL, as shown in Fig. 7(b) [31]. The transfer function of the input ($\Delta\omega_g$) to the output angular frequency ($\Delta\hat{\omega}_g$) for SOGI-FLL is given in (26), and its parameters are tuned following [31]:

$$\begin{cases} G_{FLL}(s) = \frac{\Delta\hat{\omega}_g(s)}{\Delta\omega_g(s)} = \frac{\omega_{n-FLL}^2}{s^2 + 2\xi_{FLL} \omega_{n-FLL} s + \omega_{n-FLL}^2} \\ \omega_{n-FLL}^2 = 0.5K_{i-FLL}, \quad \xi_{FLL} = \frac{0.25 K_{p-FLL} \omega_0}{\omega_{n-FLL}} \end{cases} \quad (26)$$

In (26), K_{p-FLL} and K_{i-FLL} are the proportional and integral gains of the SOGI-FLL, respectively, which are designed to achieve the desired damping factor (ξ_{FLL}) and natural frequency (ω_{n-FLL}) [31]. The detailed parameter design guideline is provided in Appendix B.

For the proposed strategy, a simple R controller is employed for inertia provision as it offers a better inertial response compared to both PR and PRR controllers. In fact, while PR and PRR are designed to add damping, both compromise inertial characteristics. It will be shown that the proposed damping strategy maintains the strong inertial performance of the simple R controller while providing significantly more effective damping than both PR and PRR controllers.

Fig. 6(b) shows the relationship between the measured current and the input of the AHO strategy with both the SOGI and virtual inertia effect. The relationship between the SOGI's output amplitude (\bar{Y}) and its input (\bar{I}) is obtained in (20). Additionally, the relationship between the R controller's output amplitude (\bar{Y}') and its input (\bar{I}_{er}) is obtained in Appendix A (45). According to Fig. 7(a), the control law of the proposed strategy can be written as

$$\begin{cases} \dot{v}_\alpha = \mu (V_{p0}^2 - V_p^2) v_\alpha - \omega'_0 v_\beta - \eta y'_\beta \\ \dot{v}_\beta = \omega'_0 v_\alpha + \mu (V_{p0}^2 - V_p^2) v_\beta + \eta y'_\alpha \end{cases} \quad (27)$$

where $y'_\alpha = \bar{Y}' \cos(\theta + \delta)$ and $y'_\beta = \bar{Y}' \sin(\theta + \delta)$. According to (22), the dynamic of θ can be obtained as

$$\dot{\theta} = \omega'_0 + \frac{\eta \bar{Y}'}{V_p} (\cos(\theta + \delta) \cos(\theta) + \sin(\theta + \delta) \sin(\theta)). \quad (28)$$

Averaging over one AC cycle and substituting \bar{Y}' from (45) in (28), and simplifying it results in

$$\dot{\theta} = \omega'_0 + \frac{\eta \bar{I}_{er}}{V_p} \cos(\delta) \frac{1}{T_f s + 1} \quad (29)$$

where $\bar{I}_{er} = I_{ref} - \bar{Y}$, according to Fig. 6(b). Substituting \bar{Y} from (20) yields

$$\dot{\theta} = \omega'_0 + \frac{1}{T_f s + 1} \frac{2\eta}{V_p^2} P_{ref} - \frac{1}{T_f s + 1} \frac{1}{T_{so} s + 1} \frac{2\eta}{V_p^2} P. \quad (30)$$

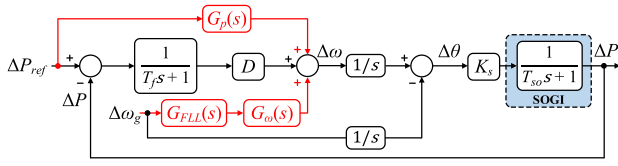


FIGURE 8. Small-signal model of the proposed strategy.

Finally, (30) can be simplified to

$$\dot{\theta} = \omega = \omega'_0 + \frac{D}{T_f s + 1} \left(P_{\text{ref}} - \frac{1}{T_{\text{so}} s + 1} P \right). \quad (31)$$

According to (25) and (31), the small-signal model of the proposed strategy can be obtained as shown in Fig. 8.

From Fig. 8, the transfer functions of the active power variations in response to fluctuations in the reference power and grid frequency can be calculated as

$$\frac{\Delta P(s)}{\Delta P_{\text{ref}}(s)} = \frac{D K_s + G_p(s) (T_f s + 1) K_s}{T_{\text{so}} T_f s^3 + (T_f + T_{\text{so}}) s^2 + s + D K_s} \quad (32a)$$

$$\frac{\Delta P(s)}{\Delta \omega_g(s)} = \frac{(G_{\text{FLL}}(s) G_{\omega}(s) - 1) (T_f s + 1) K_s}{T_{\text{so}} T_f s^3 + (T_f + T_{\text{so}}) s^2 + s + D K_s}. \quad (32b)$$

It can be seen from (32) that $G_p(s)$ ($G_{\omega}(s)$) only appears in $\Delta P(s)/\Delta P_{\text{ref}}(s)$ ($\Delta P(s)/\Delta \omega_g(s)$), so there is no coupling imposed by damping transfer functions. Therefore, proper tuning of the parameters allows independent adjustment of the dynamic responses of active power to both reference power and frequency disturbances.

Unlike the higher-order systems, the dynamic response of a standard second-order system can be simply adjusted by setting ζ and ω_n to the desired damping factor and natural frequency, respectively. Consequently, the proposed control strategy aims to shape the active power response to mimic that of a standard second-order system. This facilitates parameter design and allows the dynamic response to be tuned to a desired level, as inspired by research presented in [20] and [21]. Therefore, these two feedforward controllers will be designed such that the active power responses satisfy the following equations:

$$\frac{\Delta P(s)}{\Delta P_{\text{ref}}(s)} = \frac{\omega_{n1}^2}{s^2 + 2\zeta \omega_{n1} s + \omega_{n1}^2}. \quad (33a)$$

$$\frac{\Delta P(s)}{\Delta \omega_g(s)} = -\frac{1}{D} \frac{\omega_{n2}^2}{s^2 + 2\zeta \omega_{n2} s + \omega_{n2}^2} \quad (33b)$$

where ζ is the desired damping factor, and ω_{n1} and ω_{n2} are the desired natural frequencies of $\Delta P(s)/\Delta P_{\text{ref}}(s)$ and $\Delta P(s)/\Delta \omega_g(s)$, respectively. The primary aim of transforming from (32) to (33) is to allow the arbitrary selection of D and T_f based on the system requirements while utilizing $G_p(s)$ and $G_{\omega}(s)$ as additional design degrees of freedom to shape the dynamic response of active power in terms of ζ , ω_{n1} , and ω_{n2} . As a result, by comparing (32) and (33), $G_p(s)$ and $G_{\omega}(s)$ can

be calculated as

$$G_p(s) = \frac{a_1 s^3 + b_1 s^2 + c_1 s}{d_1 s^3 + e_1 s^2 + f_1 s + g_1} \quad (34a)$$

$$G_{\omega}(s) = \frac{a_2 s^3 + b_2 s^2 + c_2 s}{d_2 s^3 + e_2 s^2 + f_2 s + g_2} \quad (34b)$$

$$\frac{s^2 + 2\zeta_{\text{FLL}} \omega_{n-\text{FLL}} s + \omega_{n-\text{FLL}}^2}{\omega_{n-\text{FLL}}^2}$$

where

$$\begin{cases} a_1 = \omega_{n1}^2 T_{\text{so}} T_f, & b_1 = \omega_{n1}^2 (T_f + T_{\text{so}}) - D K_s \\ c_1 = \omega_{n1}^2 - D K_s 2\zeta \omega_{n1}, & a_2 = -\frac{\omega_{n2}^2 T_{\text{so}} T_f}{D} + K_s T_f \\ b_2 = -\frac{\omega_{n2}^2 (T_f + T_{\text{so}})}{D} + K_s (1 + 2\zeta \omega_{n2} T_f) \\ c_2 = -\frac{\omega_{n2}^2}{D} + K_s (T_f \omega_{n2}^2 + 2\zeta \omega_{n2}) \\ d_i = K_s T_f, & e_i = K_s (1 + 2\zeta \omega_{ni} T_f) \\ f_i = K_s (T_f \omega_{ni}^2 + 2\zeta \omega_{ni}), & g_i = K_s \omega_{ni}^2 \end{cases} \quad (35)$$

and $i = 1, 2$.

Additionally, the transfer function of $\Delta \omega(s)/\Delta P(s)$, which is relevant in stand-alone mode, is derived as follows, which confirms that the proposed damping strategy does not affect the virtual inertia characteristic:

$$\frac{\Delta \omega(s)}{\Delta P(s)} = -\frac{1}{T_f s + 1} D. \quad (36)$$

In grid-connected mode, the transfer functions of $\Delta \omega(s)/\Delta P_{\text{ref}}(s)$ and $\Delta \omega(s)/\Delta \omega_g(s)$ can be calculated as

$$\frac{\Delta \omega(s)}{\Delta P_{\text{ref}}(s)} = \frac{(s^2 + 2\zeta \omega_{n1} s) D}{(s^2 + 2\zeta \omega_{n1} s + \omega_{n1}^2) (T_f s + 1)} + G_p(s) \quad (37a)$$

$$\frac{\Delta \omega(s)}{\Delta \omega_g(s)} = \frac{\omega_{n2}^2}{(s^2 + 2\zeta \omega_{n2} s + \omega_{n2}^2) (T_f s + 1)} + G_{\text{FLL}}(s) G_{\omega}(s). \quad (37b)$$

Since the numerator and denominator of $G_p(s)$ and $G_{\text{FLL}}(s) G_{\omega}(s)$ have the same order, the angular frequency shows an initial jump ($\Delta \omega(0+) \neq 0$), causing a high initial RoCoF in response to variations in both active power reference and grid frequency. To address this, a simplification can be performed on $G_p(s)$ and $G_{\omega}(s)$ by neglecting the nondominant zeros. From (34a), the zeros of $G_p(s)$ are given in the following equation:

$$\begin{cases} Z_1 = 0 \\ Z_{2,3} = \frac{-b_1 \pm \sqrt{b_1^2 - 4a_1 c_1}}{2a_1} \end{cases} \quad (38)$$

Fig. 9(a) shows the value of $|Z_2/Z_3|$ versus ω_{n1} for the parameters in Table 1. It can be seen that when $\omega_{n1} < 10$ rad/s, $|Z_2| \gg |Z_3|$, thus, $G_p(s)$ can be approximated by the following equation:

$$\begin{cases} G_p(s) \approx \frac{b'_1 s^2 + c_1 s}{d_1 s^3 + e_1 s^2 + f_1 s + g_1} \\ b'_1 = \frac{b_1 - \sqrt{b_1^2 - 4a_1 c_1}}{2} \end{cases} \quad (39)$$

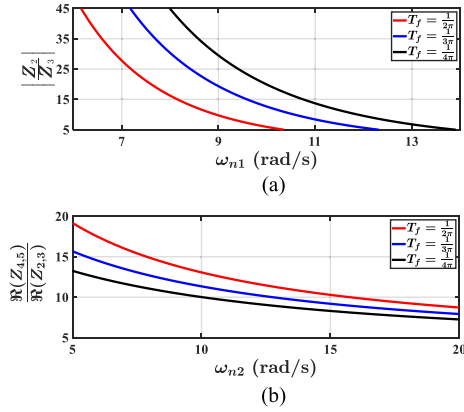


FIGURE 9. Ratio of nondominant to dominant zeros for (a) $G_p(s)$ and (b) $G_w(s)$.

Similarly, zeros of $G_w(s)$ can be obtained as

$$\begin{cases} Z_1 = 0, Z_{2,3} = \frac{-b_2 \pm \sqrt{b_2^2 - 4a_2c_2}}{2a_2} \\ Z_{4,5} = -\xi_{\text{FLL}} \omega_{n-\text{FLL}} \pm j \omega_{n-\text{FLL}} \sqrt{1 - \xi_{\text{FLL}}^2} \end{cases} \quad (40)$$

Fig. 9(b) shows the ratio of the real part of $Z_{4,5}$ ($(Z_{4,5})$) to the real part of $Z_{2,3}$ ($(Z_{2,3})$) as a function of ω_{n2} . Clearly, $Z_{4,5}$ can be safely neglected as always $|Z_{4,5}| \gg |Z_{2,3}|$ and $G_w(s)$ can be approximated as

$$G_w(s) \approx \frac{a_2 s^3 + b_2 s^2 + c_2 s}{d_2 s^3 + e_2 s^2 + f_2 s + g_2} \quad (41)$$

Replacing (39) and (41) into (37) and using the initial value theorem results in the following equations, which confirms that the initial jumps are avoided, resulting in a significantly lower initial RoCoF:

$$\Delta\omega(0+) = \lim_{s \rightarrow \infty} s \frac{\Delta\omega(s)}{\Delta P_{\text{ref}}(s)} \frac{1}{s} = 0 \quad (42a)$$

$$\Delta\omega(0+) = \lim_{s \rightarrow \infty} s \frac{\Delta\omega(s)}{\Delta\omega_g(s)} \frac{1}{s} = 0. \quad (42b)$$

Finally, the parameters of the proposed strategy can be tuned according to the desired dynamic response. For well-damped responses, ζ is generally set to values greater than 0.7 [21]. As a result, $\zeta = 0.85$, $\omega_{n1} = 2\pi$ rad/s, and $\omega_{n2} = 4\pi$ rad/s are selected. It is worth noting that when designing ω_{n1} , its effect on the values of $|Z_2/Z_3|$ in Fig. 9(a) should be considered.

C. STABILITY ANALYSIS

This section examines the impact of various parameters on the stability of the proposed control strategy. To do this, the trajectory of dominant poles for $\Delta P(s)/\Delta P_{\text{ref}}(s)$ and $\Delta P(s)/\Delta\omega_g(s)$ is plotted under variations in ζ , ω_{n1} , and ω_{n2} . Fig. 10(a) and (b) demonstrates the closed-loop poles of $\Delta P(s)/\Delta P_{\text{ref}}(s)$ and $\Delta P(s)/\Delta\omega_g(s)$ for ζ ranging from 0.6 to 1, respectively. The results reveal that poles p_1 , p_2 , and p_3 remain unchanged regardless of ζ , whereas p_4 and p_5 , associated with the damping strategy, are adjusted to achieve the desired damping factor.

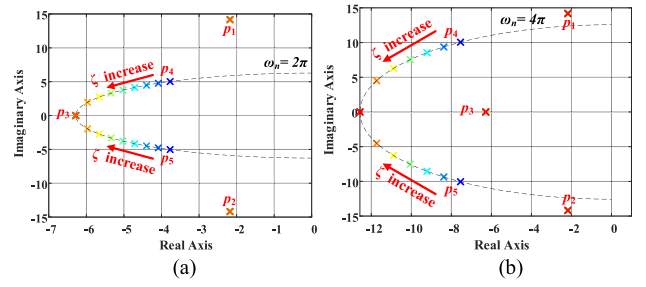


FIGURE 10. Closed-loop poles of (a) $\Delta P(s)/\Delta P_{\text{ref}}(s)$ and (b) $\Delta P(s)/\Delta\omega_g(s)$ when ζ changes from 0.6 to 1.

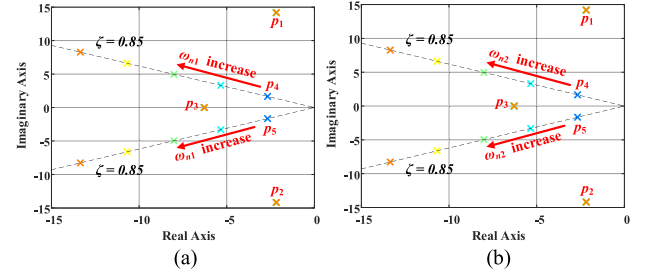


FIGURE 11. Closed-loop poles of (a) $\Delta P(s)/\Delta P_{\text{ref}}(s)$ and (b) $\Delta P(s)/\Delta\omega_g(s)$ when ω_{n1} and ω_{n2} change from π to 5π .

The closed-loop poles of $\Delta P(s)/\Delta P_{\text{ref}}(s)$ and $\Delta P(s)/\Delta\omega_g(s)$ are shown in Fig. 11(a) and (b), when ω_{n1} and ω_{n2} vary from π to 5π , respectively. Similar to ζ , these parameters primarily influence p_4 and p_5 , which shift along the $\zeta = 0.85$ line, consistent with the parameter design. Based on these observations, it can be concluded that since the proposed controller shapes the active power loop to a standard second-order system, poles p_4 and p_5 stay in the left-half plane for $0 < \zeta < 1$ and $\omega_n > 0$.

Furthermore, variations in the AHO's parameter η and T_f , as well as the grid inductance L_g , only affect the poles p_1 , p_2 , and p_3 . Since the proposed controller employs a feedforward strategy, these poles behave similarly to the conventional R controller described in [18]. Therefore, the proposed strategy does not compromise the stability of the conventional controller.

D. COMPARISON WITH CONVENTIONAL METHODS

This section compares the performance of the proposed strategy with the conventional R and PR controllers. Fig. 12 shows the step response of $\Delta\omega(s)/\Delta P(s)$, $\Delta P(s)/\Delta P_{\text{ref}}(s)$, and $\Delta P(s)/\Delta\omega_g(s)$ for the parameters listed in Table 1. Fig. 12(a) compares the inertial response in stand-alone mode. It can be seen that, unlike the PR controller, the proposed method does not compromise the virtual inertia of the simple R controller. Fig. 12(b) and (c) shows that, in contrast to the conventional R controller, the proposed strategy effectively mitigates the overshoot and oscillations caused by both active power reference and grid frequency changes. A slight deviation from the standard second-order system can be observed in Fig. 12(c), which is attributed to the simplification of (39).

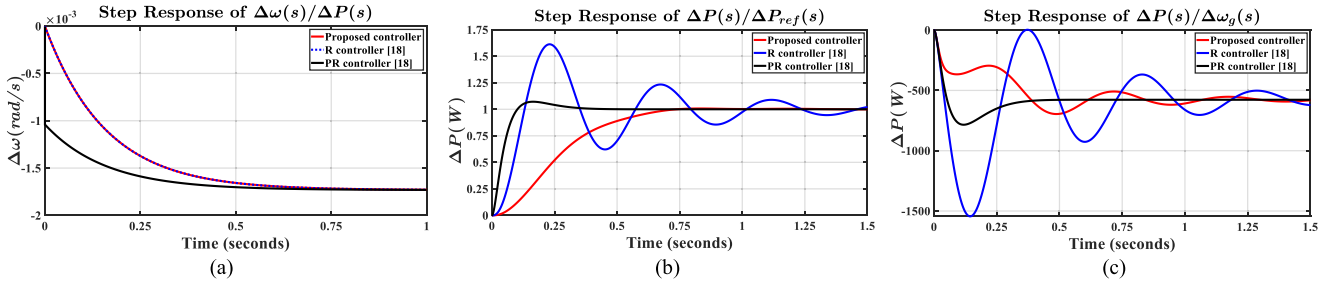


FIGURE 12. Step response comparison of (a) $\Delta\omega(s)/\Delta P(s)$, (b) $\Delta P(s)/\Delta P_{ref}(s)$, and (c) $\Delta P(s)/\Delta\omega_g(s)$.

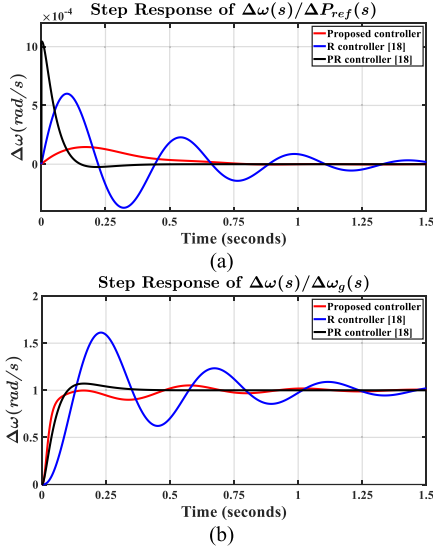


FIGURE 13. Step response comparison of (a) $\Delta\omega(s)/\Delta P_{ref}(s)$ and (b) $\Delta\omega(s)/\Delta\omega_g(s)$.

Fig. 13 shows the step responses of $\Delta\omega(s)/\Delta P_{ref}(s)$ and $\Delta\omega(s)/\Delta\omega_g(s)$. In Fig. 13(a), the proposed strategy exhibits a lower RoCoF, a reduced peak frequency, fewer low-frequency oscillations, and a higher nadir frequency than the other controllers when the power reference changes. In this figure, a significant initial RoCoF is evident for the PR controller due to the added zero to its transfer function. Additionally, Fig. 13(b) shows a lower oscillation and frequency peak for the proposed strategy when the grid frequency deviates from its nominal value.

IV. EXPERIMENTAL VERIFICATION

To validate the effectiveness of the proposed strategy, the block diagrams in Figs. 1 and 7 are implemented as shown in Fig. 14, using the parameters listed in Table 1. The Cinerga 7.5 kVA grid emulator is employed to simulate the grid behavior. The AHO control algorithm is implemented on the dSPACE DS1007 real-time system. The measured inverter's current and voltages are sent to the dSPACE platform via the DS2004 A/D Board. Additionally, pulsewidth modulation and the relay's ON-OFF signals come from the DS4002 digital IO Board. The calculated active power (P) and the

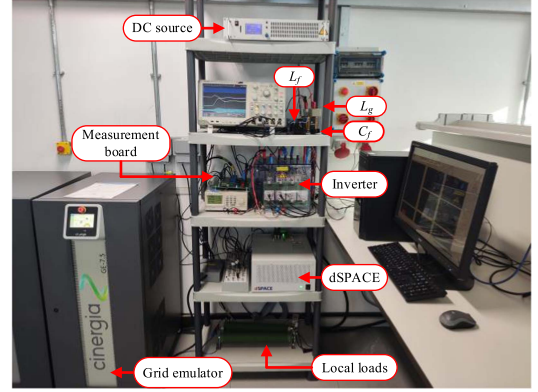


FIGURE 14. Experimental test setup.

inverter's frequency deviation from its nominal value ($\Delta f = f - 50$) are sent to the Tektronix MSO 5204B oscilloscope via the DS2101 D/A Board. For all experimental tests, the instantaneous power is calculated by multiplying the measured voltage v_{pcc} by the output current. The active power is then obtained using an averaging method in dSPACE to filter instantaneous power fluctuations inherent in single-phase systems. Furthermore, the frequency of all control strategies is uniformly calculated using their respective droop equations, as defined in (6) and (31).

Theoretical results are confirmed through five different test scenarios. In Case 1, the inverter with virtual inertia operates in stand-alone mode, where its dynamic responses to the load changes are compared. In Cases 2 and 3, the inverter is in grid-connected mode to compare the responses to power reference and grid frequency changes, respectively. The performance of the proposed strategy is further investigated in Cases 4 (stand-alone, inductive, and rectifier load) and 5 (weak grid conditions).

A. CONVENTIONAL R CONTROLLER

Typically, the inertial response of GFM inverters is evaluated in stand-alone mode by observing frequency dynamics in response to load changes. Accordingly, in Case 1, the inverter operates in stand-alone mode to demonstrate its virtual inertia provision. Before the load change, the inverter supplies only $R_{L1} = 100 \Omega$, with an output active power of about 480 W. Subsequently, $R_{L2} = 33 \Omega$ is added in parallel, increasing the

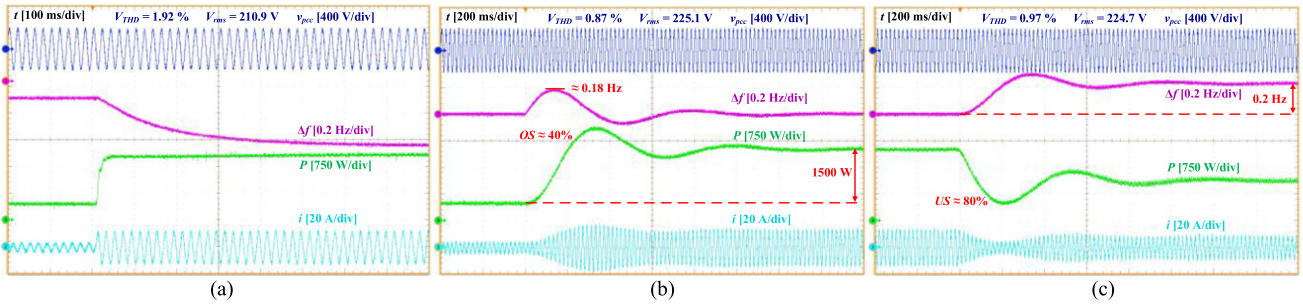


FIGURE 15. Experimental results of the conventional R controller. (a) Case 1. (b) Case 2. (c) Case 3.

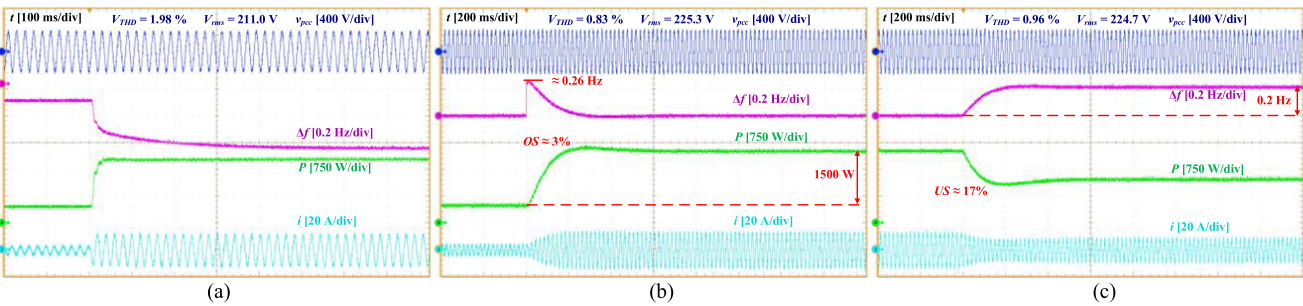


FIGURE 16. Experimental results of the conventional PR controller. (a) Case 1. (b) Case 2. (c) Case 3.

output power to about 1800 W. Fig. 15(a) shows these results, confirming that the R controller provides adequate virtual inertia with a RoCoF of 3.2 Hz/s, consistent with the theoretical step responses of $\Delta\omega(s)/\Delta P(s)$ in Fig. 12(a). These results validate the design procedure for T_f .

In Case 2, the AHO-based inverter operates in grid-connected mode. To evaluate its dynamic behavior under a power reference change, P_{ref} is jumped from 500 W to 2 kW. Fig. 15(b) shows the experimental waveforms, revealing a 40% power OS, which exceeds practical limits. Additionally, the frequency response exhibits low-frequency oscillations, with peak and nadir values of 50.18 Hz and 49.94 Hz, respectively.

Fig. 15(c) shows the experimental results for Case 3, where the grid frequency changes from 50 Hz to 50.2 Hz while $P_{\text{ref}} = 2$ kW. Similar to Case 2, a significant US of 80% is observed, posing potential risks to power electronic components. Interestingly, the experimental OS/US is lower than theoretical predictions, primarily due to parasitic resistances present in the hardware setup. Nevertheless, both theoretical and experimental results exhibit excessive OS/US.

In summary, the experimental results for the conventional R controller confirm that the selected T_f effectively limits RoCoF within the acceptable range. However, power OS/US levels exceed the practical criteria, consistent with theoretical predictions in Fig. 12.

B. CONVENTIONAL PR CONTROLLER

Following a similar approach, the theoretical performance of the PR controller is examined through three test scenarios.

Fig. 16(a) shows the results for Case 1, indicating a faster frequency response and reduced virtual inertia compared to the R controller. This results in a RoCoF of 6.3 Hz/s, surpassing practical limits set by grid operators. Additionally, a considerable initial RoCoF in the PR controller can trigger the protections.

In Cases 2 and 3, shown in Fig. 16(b) and (c), power OS and US levels are reduced to 3% and 17%, respectively. This confirms that the selected $K_p = 0.6$ successfully keeps transient power deviations within acceptable limits for power electronic converters. However, as already expected from Fig. 13(a), a considerable initial RoCoF can be seen in Fig. 16(b), much beyond the standard requirements, leading to grid frequency instability [32].

In summary, the experimental results validate that, while the PR controller with the chosen K_p effectively reduces power OS/US, its RoCoF remains above practical thresholds, consistent with theoretical predictions in Figs. 12 and 13.

C. PROPOSED DAMPING STRATEGY

This section evaluates the proposed damping strategy across five test scenarios. In Case 1, shown in Fig. 17(a), the results confirm that the proposed strategy, like the R controller, provides adequate virtual inertia, maintaining a RoCoF of 3.2 Hz/s within acceptable practical limits. Furthermore, this figure shows that the steady-state performance of the proposed and conventional controllers is the same, with frequency values of about 49.87 Hz and 49.52 Hz before and after the load change, respectively. This shows that the proposed

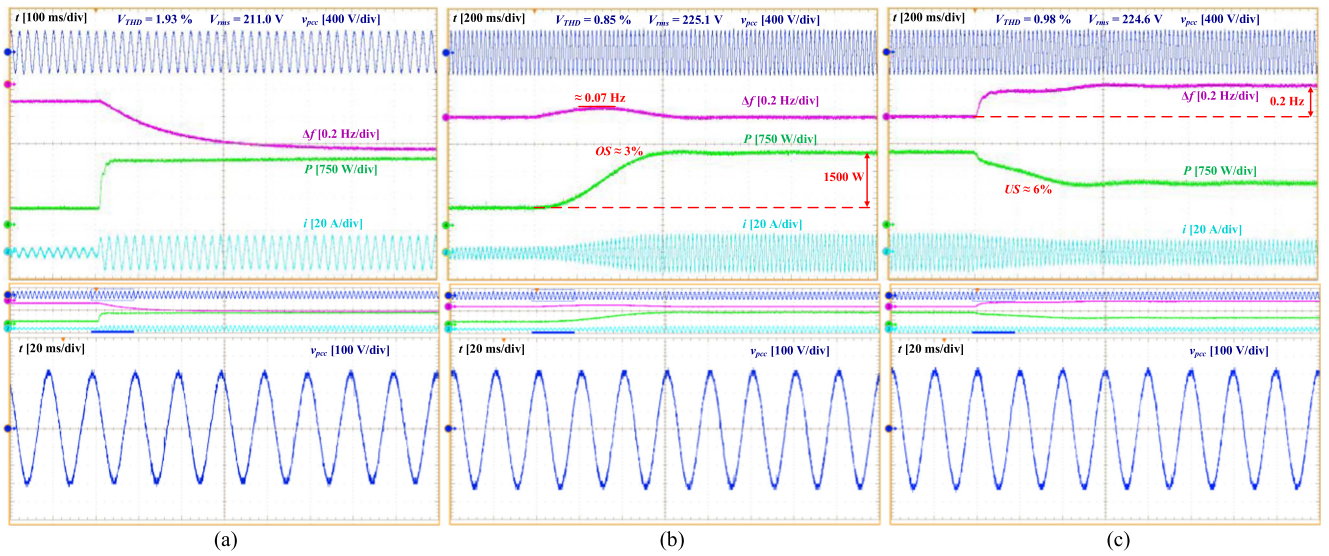


FIGURE 17. Experimental results of the proposed controller. (a) Case 1. (b) Case 2. (c) Case 3.

TABLE 2. Comparison Between Proposed and Conventional Strategies Based on Theoretical and Experimental Results

Strategies		R controller [18]		PR controller [18]		Proposed controller		Practical limits
		Experiment	Theory	Experiment	Theory	Experiment	Theory	
Case 1	RoCoF (Hz/s)	3.2	3.3	5	6.66	3.2	3.3	3.5
	Initial RoCoF (Hz/s)	0	0	∞	∞	0	0	0
Case 2	Power OS (%)	40	48	3	5	3	7	20
	RoCoF (Hz/s)	1.5	1.42	∞	∞	0.30	0.21	3.5
	Initial RoCoF (Hz/s)	0	0	∞	∞	0	0	0
	Nadir frequency (Hz)	49.94	49.93	49.98	49.99	50	50	--
	Peak Frequency (Hz)	50.18	50.14	50.26	50.24	50.07	50.04	--
Case 3	Power US (%)	80	140	17	27	6	10	20
	RoCoF (Hz/s)	1.65	1.39	1.5	1.22	2.3	1.9	3.5
	Initial RoCoF (Hz/s)	0	0	0	0	0	0	0
	Peak frequency (Hz)	50.27	50.32	50.22	50.23	50.22	50.21	--

Values highlighted in green indicate the best performance, while values in red represent the worst performance.

strategy does not affect the steady-state performance of the conventional controllers.

The results of Case 2 in Fig. 17(b) demonstrates that the proposed strategy provides a well-damped output power with negligible OS or oscillations. Additionally, a smoother frequency response can be seen with a peak value of 50.07 Hz.

For Case 3, Fig. 17(c) illustrates the proposed strategy's effectiveness in damping transient responses, achieving a minor US of 6% and a smoother current waveform transient. Steady-state output power transitions from 2000 W to 1200 W for all three controllers, confirming that the proposed damping method preserves the steady-state droop characteristics of the AHO.

In addition to transient performance, Fig. 17 includes zoomed views of v_{pcc} . These results demonstrate that v_{pcc} remains unchanged during transients, verifying GFM

operation. Moreover, comparisons of voltage total harmonic distortion (v_{THD}) and RMS values (V_{rms}), reported on the waveforms across different strategies, reveal similar values, indicating that the proposed strategy does not affect steady-state operating points or voltage waveform quality.

Table 2 compares the measured results from experiments and the theoretical values against the practical criteria for the R, PR, and proposed controllers. The results show that the experimental measurements are consistent with the theoretical predictions. Furthermore, unlike the conventional controllers, the proposed strategy addresses all practical requirements at the same time.

As a GFM inverter, the proposed strategy should be capable of generating and maintaining a regulated AC voltage regardless of the load type. To validate this, in Case 4, two experiments are conducted to supply RL and rectifier loads.

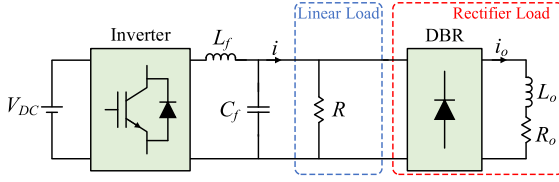


FIGURE 18. Stand-alone operation of the proposed strategy to supply linear and rectifier loads.

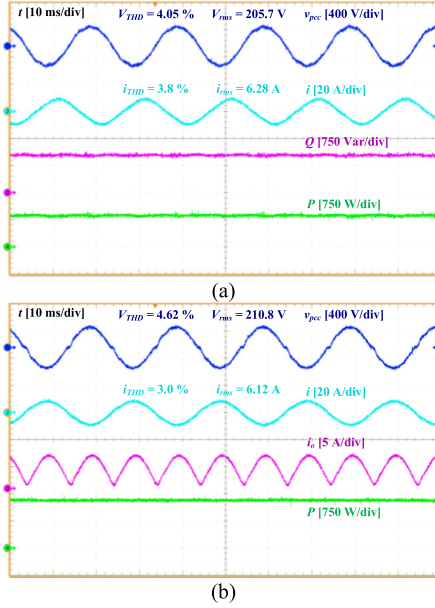


FIGURE 19. Experimental results of Case 4. (a) RL. (b) Rectifier load.

In the first test, the proposed strategy supplies an RL load with $L=35$ mH and $R=16$ Ω , designed to deliver 900 W of active power and 1000 var of reactive power. In the second scenario, as shown in Fig. 18, the proposed strategy supplies both linear load ($R=100$ Ω) and rectifier load, as done in [33]. The rectifier load consists of a single-phase diode bridge rectifier supplying an RL load, with $L_o=15$ mH and $R_o=47$ Ω . Fig. 19(a) shows the experimental waveforms for the RL load case, demonstrating a voltage amplitude of 206 V and a THD of 4.05%, and a current amplitude and THD of 6.28 A and 3.8%, respectively. For the rectifier load case, Fig. 19(b) shows the experimental results. As expected, the introduction of a rectifier load generates harmonic distortions, consistent with observations in other GFM inverters under similar conditions [33]. The measured voltage THD is 4.62%, which remains within the IEEE Std. 1547 limit [33]. Additionally, this figure shows the corresponding current waveform, with a measured THD of 3% and an amplitude of 6.12 A, confirming that the proposed strategy achieves low-harmonic current waveforms even under rectifier load conditions.

Since the proposed strategy employs an SOGI-FLL, its performance in weak grids should be examined. To do this, in Case 5, experiments in Cases 2 and 3 were repeated for the

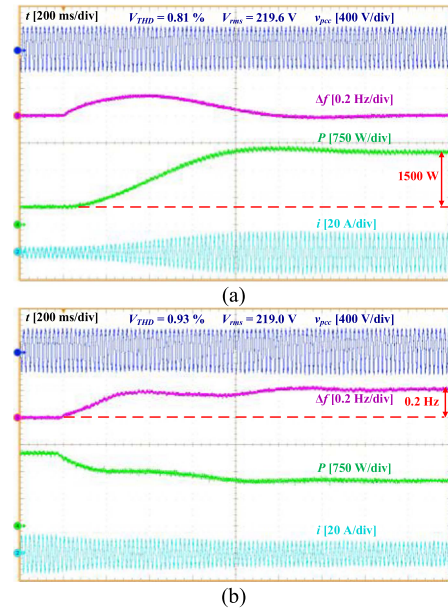


FIGURE 20. Experimental results of Case 5: step jump in (a) P_{ref} and (b) f_g .

proposed strategy with the grid inductance $L_g = 15$ mH, to emulate a weak grid. Fig. 20(a) shows the results when P_{ref} is jumped from 500 W to 2 kW. Additionally, the response to the grid frequency changes from 50 to 50.2 Hz when $P_{ref} = 2$ kW is shown in Fig. 20(b). Both tests confirm the stable operation and effective oscillation mitigation of the proposed strategy under weak grid conditions.

V. CONCLUSION

This article presents a novel damping improvement strategy for single-phase VOC-based inverters, addressing the critical challenge of enhancing damping without compromising the virtual inertia or droop control functionalities. By investigating the impact of a fictitious phase generator on the inverter's dynamic response and employing a feedforward approach, the proposed method successfully mitigates oscillations caused by power reference changes and grid frequency deviations without sacrificing virtual inertia. Theoretical and experimental results consistently confirm that the proposed strategy provides smoother power and frequency responses in grid-connected mode while maintaining adequate virtual inertia in stand-alone operation. Key advantages of the proposed strategy over conventional controllers include reduced peak frequency, lower initial RoCoF, minimized OS/US, diminished power and frequency oscillations, and higher frequency nadir in grid-connected mode, as well as a lower RoCoF in stand-alone operation.

APPENDIX A INERTIAL EFFECT DERIVATION OF RESONANT CONTROLLERS

Equation (6) can be derived using the state-space representation of (5). For the R controller with transfer function in (5a),

the state-space equations can be obtained as

$$\begin{cases} \dot{x}'_1 = \omega_0 x'_2 \\ \dot{x}'_2 = -\omega_0 x'_1 - 2\omega_f x'_2 + 2\omega_f i_{er} \\ \dot{y}' = x'_2 \end{cases} \quad (43)$$

where $x'_1 = X' \sin(\gamma')$, $x'_2 = X' \cos(\gamma')$, and $i_{er} = I_{er} \cos(\gamma')$. Fig. 6(b) shows the relationship between the measured current and the input of the AHO strategy. Since the SOGI effect was not accounted for in conventional strategies, the small-signal model in Fig. 3 was derived without incorporating the SOGI effect. By defining $X' = \sqrt{x_1'^2 + x_2'^2}$, its time derivative is

$$\dot{X}' = \frac{x'_1 \dot{x}'_1 + x'_2 \dot{x}'_2}{X'} = -2\omega_f X' \cos^2(\gamma') + 2\omega_f I_{er} \cos^2(\gamma'). \quad (44)$$

By averaging over one AC cycle and considering $Y' = X'$ from (43), we can write

$$\frac{\bar{Y}'(s)}{\bar{I}_{er}(s)} = \frac{\omega_f}{s + \omega_f} = \frac{1}{T_f s + 1}. \quad (45)$$

From Fig. 1, the control law of AHO by considering the effect of virtual inertia can be obtained as

$$\begin{cases} \dot{v}_\alpha = \mu(V_{p0}^2 - V_p^2)v_\alpha - \omega_0 v_\beta - \eta y'_\beta \\ \dot{v}_\beta = \omega_0 v_\alpha + \mu(V_{p0}^2 - V_p^2)v_\beta + \eta y'_\alpha \end{cases} \quad (46)$$

According to (22), the dynamic equation of θ can be expressed as

$$\dot{\theta} = \omega_0 + \frac{\eta Y'}{V_p} (\cos(\theta + \delta) \cos(\theta) + \sin(\theta + \delta) \sin(\theta)). \quad (47)$$

Averaging over one AC cycle and substituting \bar{Y}' from (45) in (47), and simplifying it results in

$$\dot{\theta} = \omega_0 + \frac{\eta \bar{I}_{er}}{V_p} \cos(\delta) \frac{1}{T_f s + 1} \quad (48)$$

where $\bar{I}_{er} = I_{ref} - \bar{I}$. Thus

$$\dot{\theta} = \omega_0 + \frac{1}{T_f s + 1} D (P_{ref} - P). \quad (49)$$

Using a similar approach for the PR and PRR controller, the dynamic equation of $\bar{\theta}$ for the conventional controllers can be obtained as a general form of (6), where $G_{VI}(s)$ is given by (7).

APPENDIX B

SOGI-FLL PARAMETER DESIGN

The parameters K_{p-FLL} and K_{i-FLL} are calculated to achieve the desired damping factor (ζ_{FLL}) and natural frequency (ω_{n-FLL}). The parameters ζ_{FLL} and ω_{n-FLL} are chosen based on the following requirements [31].

- 1) ζ_{FLL} should be selected to ensure sufficient damping. In practice, $\zeta_{FLL} > 0.7$ is recommended. In this article, $\zeta_{FLL} = 0.9$ is chosen.
- 2) ω_{n-FLL} primarily determines the bandwidth and, therefore, the speed of the SOGI-FLL's dynamic response. Increasing ω_{n-FLL} enhances the response speed and

reduces the effect of the SOGI-FLL's dynamic response on the proposed control strategy. However, high ω_{n-FLL} can reduce noise immunity and degrade stability. In this article, $\omega_{n-FLL} = 150$ rad/s is chosen as a compromise between bandwidth and noise immunity.

Therefore, according to (26), K_{p-FLL} and K_{i-FLL} can be calculated as

$$\begin{cases} K_{p-FLL} = \frac{4 \xi_{FLL} \omega_{n-FLL}}{\omega_0} = 1.72 \\ K_{i-FLL} = 2 \omega_{n-FLL}^2 = 45\,000 \end{cases} \quad (50)$$

REFERENCES

- [1] B. Muftau and M. Fazeli, "The role of virtual synchronous machines in future power systems: A review and future trends," *Elect. Power Syst. Res.*, vol. 206, May 2022, Art. no. 107775, doi: [10.1016/j.epsr.2022.107775](https://doi.org/10.1016/j.epsr.2022.107775).
- [2] N. Mohammed, H. Udawatte, W. Zhou, D. Hill, and B. Bahrani, "Grid-forming inverters: A comparative study of different control strategies in frequency and time domains," *IEEE Open J. Ind. Electron. Soc.*, vol. 5, pp. 185–214, 2024, doi: [10.1109/OJIES.2024.3371985](https://doi.org/10.1109/OJIES.2024.3371985).
- [3] S. Luo, W. Chen, Z. Hao, and Y. Wang, "A transient stability enhanced Andronov–Hopf oscillator for grid-forming converters," *IEEE Trans. Power Electron.*, vol. 39, no. 9, pp. 10853–10864, Sep. 2024, doi: [10.1109/TPEL.2024.3404426](https://doi.org/10.1109/TPEL.2024.3404426).
- [4] H. Zhang, W. Xiang, W. Lin, and J. Wen, "Grid forming converters in renewable energy sources dominated power grid: Control strategy, stability, application, and challenges," *J. Mod. Power Syst. Clean Energy*, vol. 9, no. 6, pp. 1239–1256, 2021, doi: [10.35833/MPCE.2021.000257](https://doi.org/10.35833/MPCE.2021.000257).
- [5] Z. Shi, J. Li, H. I. Nurdin, and J. E. Fletcher, "Comparison of virtual oscillator and droop controlled islanded three-phase microgrids," *IEEE Trans. Energy Convers.*, vol. 34, no. 4, pp. 1769–1780, Dec. 2019, doi: [10.1109/TEC.2019.2922447](https://doi.org/10.1109/TEC.2019.2922447).
- [6] H. Yu, M. A. Awal, H. Tu, I. Husain, and S. Lukic, "Comparative transient stability assessment of droop and dispatchable virtual oscillator controlled grid-connected inverters," *IEEE Trans. Power Electron.*, vol. 36, no. 2, pp. 2119–2130, Feb. 2021, doi: [10.1109/TPEL.2020.3007628](https://doi.org/10.1109/TPEL.2020.3007628).
- [7] B. B. Johnson, S. V. Dhople, A. O. Hamadeh, and P. T. Krein, "Synchronization of parallel single-phase inverters with virtual oscillator control," *IEEE Trans. Power Electron.*, vol. 29, no. 11, pp. 6124–6138, Nov. 2014, doi: [10.1109/TPEL.2013.2296292](https://doi.org/10.1109/TPEL.2013.2296292).
- [8] B. B. Johnson, M. Sinha, N. G. Ainsworth, F. Dorfler, and S. V. Dhople, "Synthesizing virtual oscillators to control islanded inverters," *IEEE Trans. Power Electron.*, vol. 31, no. 8, pp. 6002–6015, Aug. 2016, doi: [10.1109/TPEL.2015.2497217](https://doi.org/10.1109/TPEL.2015.2497217).
- [9] M. Lu, S. Dutta, V. Purba, S. Dhople, and B. Johnson, "A grid-compatible virtual oscillator controller: Analysis and design," in *Proc. IEEE Energy Convers. Congr. Expo.*, 2019, pp. 2643–2649, doi: [10.1109/ECCE.2019.8913128](https://doi.org/10.1109/ECCE.2019.8913128).
- [10] M. Lu, "Virtual oscillator grid-forming inverters: State of the art, modeling, and stability," *IEEE Trans. Power Electron.*, vol. 37, no. 10, pp. 11579–11591, Oct. 2022, doi: [10.1109/TPEL.2022.3163377](https://doi.org/10.1109/TPEL.2022.3163377).
- [11] M. Lu, S. Dhople, and B. Johnson, "Benchmarking nonlinear oscillators for grid-forming inverter control," *IEEE Trans. Power Electron.*, vol. 37, no. 9, pp. 10250–10266, Sep. 2022, doi: [10.1109/TPEL.2022.3162530](https://doi.org/10.1109/TPEL.2022.3162530).
- [12] M. A. Awal and I. Husain, "Unified virtual oscillator control for grid-forming and grid-following converters," *IEEE J. Emerg. Sel. Top. Power Electron.*, vol. 9, no. 4, pp. 4573–4586, Aug. 2021, doi: [10.1109/JESTPE.2020.3025748](https://doi.org/10.1109/JESTPE.2020.3025748).
- [13] S. A. Aghdam and M. Agamy, "Virtual oscillator-based methods for grid-forming inverter control: A review," *IET Renewable Power Gener.*, vol. 16, no. 5, pp. 835–855, Apr. 2022, doi: [10.1049/rpg2.12398](https://doi.org/10.1049/rpg2.12398).
- [14] J. Li, J. E. Fletcher, D. G. Holmes, and B. P. McGrath, "Developing a machine equivalent inertial response for a virtual oscillator controlled inverter in a machine-inverter based microgrid," in *Proc. IEEE Energy Convers. Congr. Expo.*, 2020, pp. 4314–4321, doi: [10.1109/ECCE44975.2020.9236073](https://doi.org/10.1109/ECCE44975.2020.9236073).
- [15] S. A. Aghdam and M. Agamy, "Adaptive virtual inertia synthesis via enhanced dispatchable virtual oscillator controlled grid-tied inverters," in *Proc. IECON –47th Annu. Conf. IEEE Ind. Electron. Soc.*, 2021, pp. 1–6, doi: [10.1109/IECON48115.2021.9589581](https://doi.org/10.1109/IECON48115.2021.9589581).

- [16] H. Rezaadeh, M. Monfared, M. Fazeli, and S. Golestan, "Providing inertial response with unified VOC for single-phase GFM inverters," in *Proc. Int. Symp. Elect., Electron. Inf. Eng.*, 2024, pp. 94–98, doi: [10.1109/ISEIE62461.2024.00025](https://doi.org/10.1109/ISEIE62461.2024.00025).
- [17] J. Liu, Y. Miura, and T. Ise, "Comparison of dynamic characteristics between virtual synchronous generator and droop control in inverter-based distributed generators," *IEEE Trans. Power Electron.*, vol. 31, no. 5, pp. 3600–3611, May 2016, doi: [10.1109/TPEL.2015.2465852](https://doi.org/10.1109/TPEL.2015.2465852).
- [18] S. Luo, W. Chen, X. Li, and Z. Hao, "A new virtual inertial strategy for Andronov–Hopf oscillator based grid-forming inverters," *IEEE J. Emerg. Sel. Top. Power Electron.*, vol. 12, no. 2, pp. 1995–2005, Apr. 2024, doi: [10.1109/JESTPE.2024.3370171](https://doi.org/10.1109/JESTPE.2024.3370171).
- [19] Z. Wang et al., "Active power oscillation suppression based on decentralized transient damping control for parallel virtual synchronous generators," *IEEE Trans. Smart Grid*, vol. 14, no. 4, pp. 2582–2592, Jul. 2023, doi: [10.1109/TSG.2022.3233121](https://doi.org/10.1109/TSG.2022.3233121).
- [20] M. Yang, Y. Wang, S. Chen, X. Xiao, and Y. Li, "Comparative studies on damping control strategies for virtual synchronous generators," *IEEE Trans. Power Del.*, vol. 39, no. 2, pp. 859–873, Apr. 2024, doi: [10.1109/TPWRD.2023.3339288](https://doi.org/10.1109/TPWRD.2023.3339288).
- [21] Y. Yu et al., "A reference-feedforward-based damping method for virtual synchronous generator control," *IEEE Trans. Power Electron.*, vol. 37, no. 7, pp. 7566–7571, Jul. 2022, doi: [10.1109/TPEL.2022.3152358](https://doi.org/10.1109/TPEL.2022.3152358).
- [22] K. R. Vasudevan, V. K. Ramachandaramurthy, T. S. Babu, and A. Pouryekta, "Synchronverter: A comprehensive review of modifications, stability assessment, applications and Future perspectives," *IEEE Access*, vol. 8, pp. 131565–131589, 2020, doi: [10.1109/ACCESS.2020.3010001](https://doi.org/10.1109/ACCESS.2020.3010001).
- [23] J. A. Suul, S. D'Arco, and G. Guidi, "Virtual synchronous machine-based control of a single-phase bi-directional battery charger for providing vehicle-to-grid services," *IEEE Trans. Ind. Appl.*, vol. 52, no. 4, pp. 3234–3244, Jul./Aug. 2016, doi: [10.1109/TIA.2016.2550588](https://doi.org/10.1109/TIA.2016.2550588).
- [24] H. Rezaadeh, M. Monfared, M. Fazeli, and S. Golestan, "Single-phase grid-forming inverters: A review," in *Proc. Int. Conf. Comput., Electron. Commun. Eng.*, 2023, pp. 7–10, doi: [10.1109/ICCECE59400.2023.10238661](https://doi.org/10.1109/ICCECE59400.2023.10238661).
- [25] D. Pan, X. Wang, F. Liu, and R. Shi, "Transient stability of voltage-source converters with grid-forming control: A design-oriented study," *IEEE J. Emerg. Sel. Topics Power Electron.*, vol. 8, no. 2, pp. 1019–1033, Jun. 2020, doi: [10.1109/JESTPE.2019.2946310](https://doi.org/10.1109/JESTPE.2019.2946310).
- [26] National Grid, "The grid code," 2024. [Online]. Available: <https://ddm.nationalenergyso.com/>
- [27] J. Rocabert, A. Luna, F. Blaabjerg, and P. Rodríguez, "Control of power converters in AC microgrids," *IEEE Trans. Power Electron.*, vol. 27, no. 11, pp. 4734–4749, Nov. 2012, doi: [10.1109/TPEL.2012.2199334](https://doi.org/10.1109/TPEL.2012.2199334).
- [28] National Grid ESO, "GC0137: Minimum specification required for provision of GB grid forming (GBGF) capability (formerly virtual synchronous machine/VSM capability)," Oct. 2021. [Online]. Available: <https://www.nationalgrideso.com/industry-information/codes/gc/modifications/gc0137-minimum-specification-required-provision-gb-grid-forming-gb-gf-capability-formerly-virtual-synchronous-machine/vsm-capability>
- [29] "ROCOF—An independent analysis on the ability of generators to ride through rate of change of frequency values up to 2 Hz/s," DNV KEMA Energy & Sustainability, Arnhem, The Netherlands, Feb. 2013. [Online]. Available: <https://cms.eirgrid.ie/independent-analysis-ability-generators-ride-through-rate-change-frequency-values-2hzs>
- [30] X. Meng, J. Liu, and Z. Liu, "A generalized droop control for grid-supporting inverter based on comparison between traditional droop control and virtual synchronous generator control," *IEEE Trans. Power Electron.*, vol. 34, no. 6, pp. 5416–5438, Jun. 2019, doi: [10.1109/TPEL.2018.2868722](https://doi.org/10.1109/TPEL.2018.2868722).
- [31] S. Golestan, J. M. Guerrero, J. C. Vasquez, A. M. Abusorrah, and Y. Al-Turki, "Standard SOGI-FLL and its close variants: Precise modeling in LTP framework and determining stability region/robustness metrics," *IEEE Trans. Power Electron.*, vol. 36, no. 1, pp. 409–422, Jan. 2021, doi: [10.1109/TPEL.2020.2997603](https://doi.org/10.1109/TPEL.2020.2997603).
- [32] A. Thommessen and C. M. Hackl, "Virtual synchronous machine control for doubly fed induction machine-based wind energy conversion systems," *IEEE Open J. Ind. Electron. Soc.*, vol. 5, pp. 264–301, 2024, doi: [10.1109/OJIES.2024.3366082](https://doi.org/10.1109/OJIES.2024.3366082).
- [33] U. C. Nwaneto and A. M. Knight, "Using dynamic phasors to model and analyze selective harmonic compensated single-phase grid-forming inverter connected to nonlinear and resistive loads," *IEEE Trans. Ind. Appl.*, vol. 59, no. 5, pp. 6136–6154, Sep./Oct. 2023, doi: [10.1109/TIA.2023.3282925](https://doi.org/10.1109/TIA.2023.3282925).



HAMED REZAADEH received the B.Sc. (Hons.) and M.Sc. (Hons.) degrees in electrical engineering from Ferdowsi University of Mashhad, Mashhad, Iran, in 2017 and 2020, respectively. He is currently working toward the Ph.D. degree in power electronics with Swansea University, Swansea, U.K.

His research interests include power electronics, renewable energy systems, and grid-forming inverters.

Mr. Rezaadeh is an active reviewer for various

IEEE transactions.



MOHAMMAD MONFARED (Senior Member, IEEE) received the M.Sc. (Hons.) and Ph.D. (Hons.) degrees in electrical engineering from Amirkabir University of Technology, Tehran, Iran, in 2006 and 2010, respectively.

Since 2022, he has been a Senior Lecturer with the Faculty of Science and Engineering, Swansea University, Swansea, U.K. His research interests include power electronics, renewable energy systems, and energy management.

Dr. Monfared is an Associate Editor for IEEE TRANSACTIONS ON INDUSTRIAL ELECTRONICS and IEEE TRANSACTIONS ON POWER ELECTRONICS, and a member of the IEEE IES Technical Committee on Renewable Energy Systems.



MEGHDAZ FAZELI (Senior Member, IEEE) received the M.Sc. and Ph.D. degrees in electrical engineering from the University of Nottingham, Nottingham, U.K., in 2006 and 2011, respectively.

From 2011 to 2012, he was a research assistant with Swansea University, recruited on an ERDF-funded project of the Solar Photovoltaic Academic Research Consortium, where he worked on integration of large PV systems, aimed to provide ancillary services. In 2013, he worked for a couple of months on the Smart Operation for Low Carbon Energy Region (SOLCER) Project as a Research Officer with Swansea University.

In 2013, he joined the Academic Staff of the Electronic and Electrical Engineering Department, Swansea University, where he is currently a Senior Lecturer. His research interests include integration and control of renewable energy, ancillary services, VSMs, energy management systems, and micro-/nanogrids.



SAEED GOLESTAN (Senior Member, IEEE) received the Ph.D. degree in electrical engineering from Aalborg University, Aalborg, Denmark, in 2018.

He is currently an Associate Professor with AAU Energy, Aalborg University. His research interests include modeling, synchronization, and control of power electronic converters and microgrids for renewable energy systems.

Prof. Golestan is currently an Associate Editor for IEEE TRANSACTIONS ON POWER ELECTRONICS, IEEE TRANSACTIONS ON INDUSTRIAL ELECTRONICS, IEEE Open Journal of the Industrial Electronics Society, and IEEE JOURNAL OF EMERGING AND SELECTED TOPICS IN POWER ELECTRONICS. He was the recipient of several awards, including the 2023 IEEE TPE Associate Editor Excellence Award and the 2022 Energies Young Award.